Journal of Neuroscience Methods xxx (xxxx) xxx–xxx

Contents lists available at ScienceDirect

Journal of Neuroscience Methods

journal homepage: www.elsevier.com/locate/jneumeth

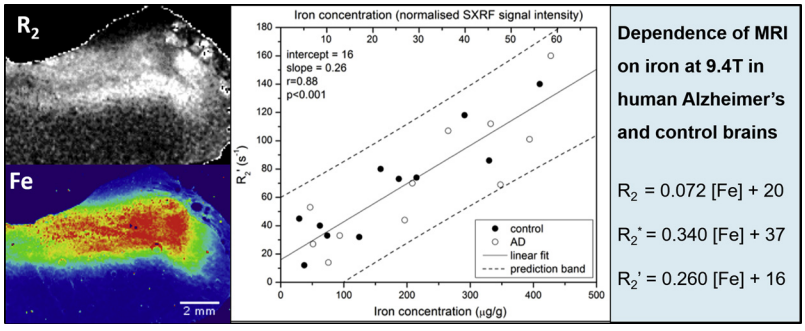
Research Article

Synchrotron XRF imaging of Alzheimer's disease basal ganglia reveals linear dependence of high-field magnetic resonance microscopy on tissue iron concentration

Mary E. Finnegan[a,b], Naomi P. Visanji[c], Isolda Romero-Canelon[d], Emily House[e], Surya Rajan[f], J. Frederick W. Mosselmans[g], Lili-Naz Hazrati[h], Jon Dobson[i], Joanna F. Collingwood[f,j,*]

[a] Department of Imaging, Imperial College Healthcare NHS Trust, London, UK
[b] Department of Bioengineering, Imperial College London, London, UK
[c] The Edmond J Safra Program in Parkinson's Disease and the Morton & Gloria Shulman Movement Disorders Clinic, Toronto Western Hospital, Toronto, Ontario, M5T 2S8, Canada
[d] School of Pharmacy, Institute of Clinical Sciences, University of Birmingham, Birmingham B15 2TT, UK
[e] Lancaster Environment Centre, Lancaster University, Lancaster, LA1 4YQ, UK
[f] School of Engineering, University of Warwick, Coventry, CV4 7AL, UK
[g] Diamond Light Source, Didcot, Oxfordshire OX11 ODE, UK
[h] The Hospital for Sick Children, Toronto, Ontario, Canada
[i] J. Crayton Pruitt Family Department of Biomedical Engineering, University of Florida, Gainesville, FL 32611, USA
[j] Department of Materials Science and Engineering, University of Florida, Gainesville, FL 32611, USA

GRAPHICAL ABSTRACT



ARTICLE INFO

Keywords:
Alzheimer's
Imaging
Iron
MRI
Relaxometry
Synchrotron
X-ray fluorescence

ABSTRACT

Background: Chemical imaging of the human brain has great potential for diagnostic and monitoring purposes. The heterogeneity of human brain iron distribution, and alterations to this distribution in Alzheimer's disease, indicate iron as a potential endogenous marker. The influence of iron on certain magnetic resonance imaging (MRI) parameters increases with magnetic field, but is under-explored in human brain tissues above 7 T.
New Method: Magnetic resonance microscopy at 9.4 T is used to calculate parametric images of chemically-unfixed post-mortem tissue from Alzheimer's cases (n = 3) and healthy controls (n = 2). Iron-rich regions including caudate nucleus, putamen, globus pallidus and substantia nigra are analysed prior to imaging of total iron distribution with synchrotron X-ray fluorescence mapping. Iron fluorescence calibration is achieved with adjacent tissue blocks, analysed by inductively coupled plasma mass spectrometry or graphite furnace atomic

* Corresponding author at: School of Engineering, University of Warwick, Coventry, CV4 7AL, UK.
E-mail address: J.F.Collingwood@warwick.ac.uk (J.F. Collingwood).

https://doi.org/10.1016/j.jneumeth.2019.03.002
Received 4 October 2018; Received in revised form 2 March 2019; Accepted 2 March 2019
0165-0270/ © 2019 The Authors. Published by Elsevier B.V. This is an open access article under the CC BY license (http://creativecommons.org/licenses/BY/4.0/).

absorption spectroscopy.
Results: Correlated MR images and fluorescence maps indicate linear dependence of R_2, R_2* and R_2' on iron at 9.4 T, for both disease and control, as follows: $[R_2(s^{-1}) = 0.072[Fe] + 20]$; $[R_2^*(s^{-1}) = 0.34[Fe] + 37]$; $[R_2'(s^{-1}) = 0.26[Fe] + 16]$ for Fe in μg/g tissue (wet weight).
Comparison with Existing Methods: This method permits simultaneous non-destructive imaging of most bioavailable elements. Iron is the focus of the present study as it offers strong scope for clinical evaluation; the approach may be used more widely to evaluate the impact of chemical elements on clinical imaging parameters.
Conclusion: The results at 9.4 T are in excellent quantitative agreement with predictions from experiments performed at lower magnetic fields.

1. Introduction

1.1. The need for biomarkers of Alzheimer's disease

Despite recent improvement in the proportion of individuals with dementia receiving a diagnosis, confirmation of a diagnosis of Alzheimer's disease is generally dependent on *post mortem* examination of the underlying disease pathology. Developments in imaging, including PET (positron emission tomography) imaging of amyloid deposition, volumetric MRI (magnetic resonance imaging) of brain atrophy and measurement of amyloid in the cerebral spinal fluid (CSF) have led to a series of proposals and recommendations to update AD diagnostic criteria e.g. (Dubois et al., 2010; McKhann et al., 2011; Dubois et al., 2016; Morris et al., 2014; Jack et al., 2013). The identification and monitoring of markers, and characterising marker profiles as a function of disease progression, remain major challenges in Alzheimer's research.

MRI is a particularly attractive diagnostic tool as it is non-invasive and does not require exposure to ionising radiation. Studies of volumetric changes in the brain have shown greater atrophy in AD subjects, but also a significant overlap with normal aging (Laakso et al., 1995; Doan et al., 2017; Habes et al., 2016; Pini et al., 2016; Wisse et al., 2014). Furthermore, atrophy indicates significant cell death has already occurred. For this reason, it is a priority to identify changes that are a precursor to irreversible atrophy, including those changes that may be detected by chemical imaging, to enable earlier diagnosis and possible future protective intervention.

1.2. Brain iron in Alzheimer's disease

Over a century ago, developments in histological methods allowed demonstration of iron in mammalian tissues, underpinning the subsequent investigation of iron and other transition metals in the human brain in health and disease (Perls, 1867). The descriptions of metal distributions throughout the cellular architecture of the brain are accompanied by quantitative post-mortem measurements of metal concentrations, such as the study of iron levels in the healthy human brain as a function of age by Hallgren and Sourander in 1958 (Hallgren and Sourander, 1958). The concentration and distribution of transition metals, including iron, are of particular interest in the context of neurodegenerative diseases. In certain rare disorders, iron dysregulation is a primary cause of mortality (Kumar et al., 2016), but in other neurodegenerative disorders the impact of observed iron dysregulation is less clear. Many studies have shown altered non-haem brain iron in specific regions of the AD brain (Samudralwar et al., 1995; Cornett et al., 1998; Loeffler et al., 1995; House et al., 2008; Thompson et al., 1988; Dedman et al., 1992; Connor et al., 1992; Deibel et al., 1996; Tao et al., 2014; Pankhurst et al., 2008; House et al., 2007; Akatsu et al., 2012; Graham et al., 2014; Hare et al., 2016; van Duijn et al., 2017), also in Parkinson's disease (Dexter et al., 1991; Oakley et al., 2007; Wang et al., 2016) and Wilson's disease (Dusek et al., 2017) amongst others. Conflicting results in the literature may be at least in part due to variability in sample archiving conditions and analytical methods, but there is undoubtedly a spectrum of 'normal' regional brain iron concentrations even taking into account variables such as health and age. The disparity is likely not fully captured in the current literature, given that studies where no significant differences between populations are observed may be unpublished or less frequently cited. In an analysis of the literature only the putamen was found to have significantly elevated iron in AD (Schrag et al., 2011). A subsequent meta-analysis by Tao and coworkers (Tao et al., 2014) evidenced elevated iron concentration in eight regions of the AD brain compared with healthy controls, specifically: frontal lobe, parietal lobe, temporal lobe, amygdala, putamen, globus pallidus, cingulate cortex, and caudate nucleus.

1.3. MRI evaluation of brain iron in Alzheimer's disease

Since the contribution of iron to MRI contrast was recognised and explored in the 1980s (Drayer et al., 1986), a number of different techniques have been developed to calculate tissue iron content in organs, including liver and heart, so that this can be used in the evaluation of patients, especially those with iron-overload disorders (St Pierre et al., 2004; Wood, 2011). Changes in non-haem iron have the potential to act as a marker of AD, because of the impact of brain tissue iron on MRI, affecting tissue susceptibility and relaxation parameters (Haacke et al., 2005). This has been demonstrated in various systems ranging from phantoms and animal models (Vymazal et al., 1992; Yang et al., 2013; Tan et al., 2014; Gossuin et al., 2004) to human post mortem tissue (House et al., 2008; Langkammer et al., 2010; Bulk et al., 2018; Antharam et al., 2012; Langkammer et al., 2012).

MR relaxometry techniques allow the quantitative mapping of the relaxation rates R_1, R_2, R_2*and related parameters (e.g. R_2'). As the transverse relaxation rate R_2, and to a lesser extent the longitudinal relaxation rate R_1, have been shown to be linearly proportional to the iron concentration at field strengths up to 7 T (Gossuin et al., 2004), MR relaxometry can provide a tool for investigating brain iron in vivo (Langkammer et al., 2014; Ghadery et al., 2015; Tang et al., 2018). A linear correlation has also been shown between R_2* and iron concentration at fields of 1.5 T – 7 T (Yao et al., 2009), with a steeper gradient (and therefore greater sensitivity) than R_2 at 3 T, the field typically used in clinical neuroimaging (Langkammer et al., 2010). As alternative and more sophisticated MRI measures of iron are developed, the well-established clinically-accessible R_2 and R_2* sequences that have been validated post-mortem retain value for the determination of iron, and offer potential to detect changes in brain iron distribution and concentration as a function of AD in critical regions such as the hippocampus and amygdala (Langkammer et al., 2014; Tang et al., 2018).

The field dependent R_2 increase (FDRI) is the degree to which the value of R_2 depends on the external magnetic field. Bartzokis and coworkers used this property to develop a means of examining iron content in R_2 MRI scans (Bartzokis et al., 1993). R_2 was obtained from dual echo sequences measured at two different field strengths; the difference calculated determined the FDRI. They showed that FDRI of the frontal white matter, caudate nucleus, putamen, and globus pallidus correlated strongly with published iron concentration values in healthy adults and with phantoms of ferritin containing agarose gels (Bartzokis et al., 1993). FDRI has since been used to study ferritin iron concentration in AD compared to control (Bartzokis et al., 1994) and also

in other neurodegenerative diseases such as Parkinson's disease and Huntington's disease (Bartzokis et al., 2004; Bartzokis and Tishler, 2000). The obvious disadvantage of FDRI is that it requires MRI mapping with two different instruments, increasing the cost and time of the imaging. It also requires careful matching of anatomical features across the two data sets. A recent publication compared FDRI obtained at 1.5 T and 4.7 T to predicted iron content from a single T_2* measurement at 4.7 T and concluded that FDRI offered few advantages over measurements at a single field (Uddin et al, 2016). Similarly, in R_2 measurements that used four single-echo acquisitions in a study of 10 healthy adults, we found that the quality of the linear relationship between R_2 and predicted iron values was only slightly more robust for FDRI using 3 T and 1.5 T, than for just the R_2 data obtained at 3 T (Collingwood et al., 2014).

Tissue degeneration, which occurs in AD, causes increased water concentration in the tissue and reduces R_2 (Bondareff et al., 1988; Bartzokis et al., 1994) in opposition to the effect of increased iron concentration. R_2' is the portion of R_2* that is caused by the dephasing of spins due to inhomogeneity of the local field, and is independent of water concentration (Yablonskiy and Haacke, 1994; Jensen and Chandra, 2000). Ordidge and co-workers developed a method for mapping R_2' that reduces the influence of background field variations and used this technique to measure an increase in iron in the SN of Parkinson's disease patients that agrees with post mortem studies, but that had not been observed in R_2 mapping (Ordidge et al., 1994). Susceptibility weighted imaging (SWI) uses a mask of phase information to enhance the contrast in an MR image. The mask can be chosen to highlight particular phases (features), so that the combined magnitude and phase information can be used, for example, to enhance contrast between grey and white matter (Haacke et al., 2004), resolve structures not observable with T_2 or T_1 weighted imaging (Manova et al., 2009) and examine the iron concentration distribution of brain tissue (Yao et al., 2009). SWI alone does not allow for quantification of the magnetic susceptibility of the tissue, and suffers from blooming artefacts (Kim et al., 2017), and developments in post-acquisition processing are enabling quantitative susceptibility mapping (QSM) to become established as a method with excellent sensitivity to iron distribution in tissue in vivo, including for the evaluation of brain iron in AD at clinically-routine field strengths (Langkammer et al., 2012; Kim et al., 2017).

The past decade has seen a significant shift from 1.5 T to 3 T MRI in clinical neuroimaging, and the ongoing move to higher field strengths brings access to increased tissue iron contrast. Early work in primate brain at fields up to 4.7 T suggested that the increased contrast would reach a threshold where the magnetisation of ferritin-bound iron became saturated (Bizzi et al., 1990). Subsequent studies in post-mortem human tissue reported a strong linear relationship was sustained between iron and R_2 at 4.7 T (House et al., 2007), and between iron and R_2* at 7 T post-mortem and *in-vivo* (Yao et al., 2009). More recent post-mortem human tissue analysis supports the use of QSM and R_2* for iron quantification in tissue at 7 T (Hametner et al., 2018; Betts et al., 2016).

We found evidence of a linear dependence of R_2 and R_2* on normalized iron concentration in post-mortem human hippocampus imaged at 14 T (Antharam et al., 2012), using synchrotron XRF (SXRF) maps to evaluate the relationship between iron distribution and these MRI parameters. As relative (rather than absolute) iron concentration was obtained, the magnitude of the field-dependent increase in R_2 and R_2* could not be tested at 14 T to determine if the effect was saturating. The present study, utilizing adjacent tissue blocks to calibrate SXRF iron maps, demonstrates one route to overcome this constraint. In the following sections, we discuss approaches to validate the relationship between clinical imaging parameters (typically MRI) and iron content in tissue.

1.4. Validating iron contrast in MRI data

Reported values for regional brain iron concentrations vary considerably, as evidenced in the landmark review by Haacke and co-workers (Haacke et al., 2005). This likely reflects a combination of natural heterogeneity in the population, and differences attributable to experimental method and study design. The field continues to be constrained by an absence of iron concentration data from large well-described cohorts. When validating MRI methods for sensitivity to iron in the brain, many studies (Bartzokis et al., 2000; Gelman et al., 1999; Persson et al., 2015; Liu et al., 2015; Gao et al., 2017; Collingwood et al., 2014) have used the data published by Hallgren and Sourander in 1958 (Hallgren and Sourander, 1958) as the definitive source of information on regional iron concentration as a function of age in the normal human brain. Comparatively few studies have quantified iron in post-mortem tissue to validate directly the relationship with the MRI parameters. To date, this has been done for R_2 and/or R_2* in studies including post-mortem human brain at fields from < 1 T up to 7 T (Vymazal et al., 1996; House et al., 2008, 2007; Langkammer et al., 2010; Yao et al., 2009; Hametner et al., 2018; Bulk et al., 2018). These studies are critical, as they do not rely on the assumption that the average iron concentration quoted in the literature accurately represents the iron in the individual(s) they are studying. However, post-mortem sample archiving and processing presents additional challenges. It is extremely rare to be in a position to work rapidly and safely with fresh human brain tissue at body temperature, and the majority of samples are either fresh-frozen and archived at −80 °C or stored in an appropriately buffered solution containing a chemical fixative such as formalin to prevent tissue deterioration. Both freezing and chemical fixation impact absolute relaxation parameters in MRI (Vymazal et al., 1996; Thelwall et al., 2006; Antharam et al., 2012), and a further complication of chemical fixation is that it can result in unpredictable levels of mineral transformation and/or metal leaching from the samples (Gellein et al., 2008; Dobson and Grassi, 1996). Some have sought to quantify the impact of iron loss in this context: Hametner and co-workers report 20% loss from in white matter, and 27% loss from putamen, after 24 days in fixative (Hametner et al., 2018). In the present study only fresh-frozen tissues were used, by following previously established protocols to enable sequential imaging analysis by MRI and SXRF (Antharam et al., 2012).

1.4.1. Validation by synchrotron X-ray fluorescence mapping

Synchrotron X-ray fluorescence mapping of biological tissues can be used to produce highly sensitive and specific maps of elemental distributions in tissue at high spatial resolution (Collingwood et al., 2005; Ugarte et al., 2012; Gallagher et al., 2012). The method offers significant advantages over histochemical staining with sensitivity to trace concentrations, specificity for the chemical elements present (e.g. unambiguous distinction between copper and zinc), and no requirement for any labelling or contrast agent. Simultaneous acquisition of the elemental spectra within a pixel, enabling a full analysis of the chemical elements present within the energy range of the instrument used, can be performed for a single tissue section (Collingwood and Adams, 2017). A number of studies have now sought to correlate MRI maps (either contrast-weighted or parametric) with post-mortem tissue sections (either chemically-fixed or fresh-frozen) analysed by SXRF, for example (Hopp et al., 2010; Antharam et al., 2012; House et al., 2014). This has enabled direct comparison of the spatial distribution of iron with MRI data. One approach is to use rapid scanning SXRF, where this is calibrated with metal foils to compare iron distribution with SWI obtained at clinical spatial resolutions at 1.5 T, evidencing a linear relationship between SWI and iron concentration in 1 mm thick fixed brain tissue (McCrea et al., 2008; Hopp et al., 2010). This approach offers the advantage of being able to cover a spatial area encompassing multiple regions of the human brain (which is not normally viable with the micro-focussed SXRF beam). However, it requires chemically fixed

samples or a cryo-environment that can accommodate large area rastering of a frozen tissue sample, and the calibration with metal foils is constrained by matrix differences between the foils and the tissues.

In the present study we incorporate a method previously developed by our group to obtain MRI and SXRF data from fresh-frozen human hippocampus at high spatial resolution (60 μm in-plane) at 14 T (Antharam et al., 2012). Here, equivalent measurements are performed for a series of brain regions from AD and healthy control cases, with the MRI analysis performed at 9.4 T. The additional step of calibrating the iron SXRF signal intensity using high precision bulk analysis of representative adjacent tissue samples permits determination of the dependence of R_2, R_2* and R_2' as a function of iron concentration, and to test the dependence of these relationships at a field exceeding 7 T.

2. Materials and methods

2.1. Samples

All tissues used in this study were from donated human brain provided by the Canadian Brain Tissue Bank and studied under ethical approval 07/MRE08/12. Tissue samples from two control (males, aged 76 and 78) and three confirmed AD cases (male, aged 73, females, aged 75 and 95) were investigated with samples taken from regions of the basal ganglia: primarily the caudate nucleus (CN), putamen (Pu), globus pallidus (GP) and substantia nigra (SN). Based on prior meta-analyses, the Pu is most likely to show increased iron concentration in AD. Where additional adjacent structures were included in MRI samples, such as the anterior limb of the internal capsule which is adjacent to the caudate nucleus, these have been segmented and included in the analysis. Case details and the samples measured for each case are given in Table 1; all samples had been stored at −80 °C. Each SXRF map took upwards of 6 h to collect, and as synchrotron beam time is limited only one section was imaged for each region per individual.

The experimental strategy was to cut pairs of blocks (adjacent tissue) from within each anatomical structure. Examples of the frozen blocks, prior to dissection, are given in Fig. 1. The first block (A) was used for MRI quantitative relaxometry and SXRF mapping, and was cut to fit inside a 20 mm diameter NMR tube. Dissection included tissue from surrounding structures to aid anatomical orientation. Block B, for iron quantification in this study by ICP-MS (where GFAAS might be used as an alternative), was selected to include only the target structure. The quantitative iron information from block B was used to calibrate the iron distribution maps from block A. As the SN anatomy is difficult to define with precision in unstained tissue, the cerebral crus was included in both samples. Where available sample volume or asymmetry prevented block B from being representative of block A (in the present study this was the case for the GP samples), the relationship between absolute iron content and SXRF signal was used to calibrate the GP images as described in section 3.1.

Before dissection, samples were warmed from archive conditions at −80 °C to a few degrees below 0 °C. They were then dissected in the temperature-controlled environment of a cryomicrotome. All sample handling was performed using acid-washed non-ferrous surfaces and tools, including ceramic blades for dissection to avoid metal particulate contamination.

2.2. Bulk iron quantification

There are several methods by which the concentration of a chemical element may be determined with great accuracy. Here we include data from two example methods that are suitable for iron determination in brain tissue. The first is inductively coupled plasma mass spectrometry (ICP-MS), here used to determine iron concentration in block B for the CN and Pu samples, and the second is graphite furnace atomic absorption spectroscopy (GFAAS) used for the equivalent blocks of SN tissue. Each method presents its own challenges, and is described in detail in the supporting references. The SN block B samples were analysed by GFAAS (instead of ICP-MS) as they were measured in the context of a study parallel to the main MRI-SXRF investigation (Visanji et al., 2013; Finnegan, 2013). Ideally the same technique and instrument would have been used to measure all the bulk iron concentrations, but the sensitivity and accuracy of these methods were sufficient (as discussed in Section 3.3.1 Method Assumptions), that here it was appropriate to pool the data for the purpose of the regression analysis.

2.2.1. Inductively coupled plasma mass spectrometry (ICP-MS)

Iron concentration was determined for the individual tissue blocks by ICP-MS, using the ICP-MS Agilent technologies 7500 series as previously described (Finnegan, 2013). Briefly, the samples were freeze dried and transferred into acid washed 3 ml capacity glass Wheaton v-vials for digestion in 72% double distilled nitric acid. A total of 1.5 ml of nitric acid was added to the vials in aliquots of 0.5 ml and then the samples were dissolved in a 55 °C oven for approximately 20 h. Each sample was diluted to 1:100 using Milli-Q® grade water (18.2 MΩ). Blanks consisting of a 1:100 dilution of the 72% nitric acid used for digestion were run after every 4 samples and consistently produced an iron concentration below the detection limit of the spectrometer.

2.2.2. Graphite furnace atomic absorption spectroscopy (GFAAS)

GFAAS was used to measure the iron concentration of the substantia nigra samples as previously described (Visanji et al., 2013). Briefly, a Mars Xpress microwave was used to digest the tissue samples in 1 ml HNO_3 and 1 ml H_2O_2 using a CEM-provided Tissue Xpress program. Ultrapure water (3 ml) was added and the digest volume corrected for venting. The iron concentration was determined from 800-fold dilutions using a hollow-cathode lamp at 30 mA and atomic absorption measured at 248.3 nm.

2.3. MRI relaxometry

MRI was performed using a Bruker micro-imaging MicWB40 probe and a 400 MHz vertical wide bore Bruker spectrometer. Each tissue sample, initially frozen, was suspended in Fluorinert in a standard glass NMR tube (Antharam et al., 2012; Finnegan, 2013). Samples were warmed to and maintained at 2 °C throughout the image acquisition, and re-frozen directly afterwards.

Before imaging, the probe was tuned and matched to the ^{1}H channel. TopSpin was used to manually shim the gradients and achieve a smooth free induction decay (FID) of maximum size, and a symmetrical, as narrow as possible water peak with a full-width-half-maximum (FWHM) of < 60 Hz. The Bruker relaxometry scans from Paravision 4.0 were used: a multi-spin, multi-echo (MSME) sequence to map T_2 and a multi-gradient echo sequence (MGE) to map T_2*. The number of averages, slice thickness and echo times were optimised to

Table 1
Case details for the samples used in this project. The sex and age of each individual at death is given. For the control cases the cause of death is stated. For the Alzheimer's Disease (AD) cases the Braak stage of the disease pathology is given (Braak and Braak, 1991). The Case References are not linked with the original numbers issued by the brain bank, they are the identifiers corresponding to the supporting analytical information for this study (Finnegan, 2013).

Case Reference	Brain regions	Sex	Age	Pathology
C2	Caudate nucleus Substantia nigra	M	78	Lung cancer
C3	Putamen Globus pallidus	M	76	Cardiac infarction
AD1	Caudate nucleus	M	73	Braak vi
AD2	Globus pallidus Substantia nigra	F	75	Braak vi
AD3	Putamen	F	98	Braak v

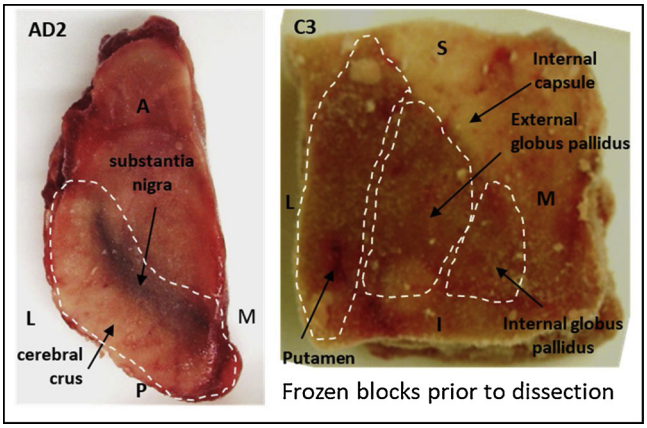


Fig. 1. Examples of the tissue blocks from the Canadian Brain Tissue Bank prior to dissection for imaging and bulk analysis, with anatomical orientations indicated (A/P: anterior/posterior; L/M: lateral/medial; S/I: superior/inferior).

give a good signal to noise ratio for even the rapid decays shown in tissue with a high iron content. The scan parameters are summarized in Table 2. Careful shimming was required to ensure optimum signal from the region of interest.

Scan geometry and workflow was similar to that described previously (Collingwood et al., 2008; Antharam et al., 2012). Low resolution scans were used first to measure the majority of the tissue sample volume. Data from these scans were then used to choose the part of the tissue to image at high resolution in order to obtain the best representation of the brain region of interest. Low resolution data were collected by three sets of scans with interleaving geometry. Two sets of interleaved high resolution scans were used to map a 7 mm thick volume of tissue.

The decays were fitted to create T_2 and T_2* maps using the open source software Image *J* with the plugins 'Bruker Opener' and 'MRI Processor'. The MRI Processor plugin was used to fit the T_2 and T_2* decays for the voxels in each respective dataset to mono-exponential Equation 1 using a Levenberg-Marquardt algorithm.

$$y = A + Ce^{(-\frac{t}{T_2})} \quad (1)$$

where the constant A takes into account a finite background. The reciprocal of the T_2 and T_2*images provided the R_2 and R_2* images respectively.

2.4. Histology

The tissue blocks that had been initially imaged by MRI microscopy were subsequently mounted to permit cryosectioning in the same plane as the virtual slices in the MRI acquisition. Sectioning was performed in a Leica cryomicrotome (Jung CM3000) at an angle of 10 ° and a nominal thickness of 30 µm. Sections were cut with an acid-washed sapphire blade to avoid metal particulate contamination from the stainless steel blades used in routine sectioning. Serial sectioning was performed, with sections for SXRF analysis mounted on spectroscopically clean quartz slides, and adjacent sections mounted on glass histology slides and stained with a standard haematoxylin and Congo red protocol (Finnegan, 2013). Only haematoxylin staining was used for the quartz sections after SXRF imaging, and initial fixation required in ice-cold ethanol (Gallagher et al., 2012), as extended imaging can render the organic material in the tissue section very fragile. This, combined with the absence of an adherent coating on the slides (to avoid a potential source of contamination) resulted in development of a staining protocol using a liquid blocking PAP pen so that sections could be individually stained with the slide maintained in a horizontal position (Finnegan, 2013).

2.5. Synchrotron X-ray fluorescence microfocus imaging

SXRF mapping of elemental metal ion distributions was performed at the microfocus beamline I18 at Diamond Light Source, following previously described protocols (Antharam et al., 2012; Gallagher et al., 2012). Briefly, a 10 keV primary beam was used to excite fluorescence from the unstained tissue section, with the incident flux I_0 limited to avoid saturation of the nine element Ge detector. The quartz-mounted sections were protected during measurement under an X-ray transparent Kapton film, and mounted with the imaging plane at 45° to I_0 and the detector at 90° to I_0. The quartz has a spatially uniform fluorescence signal making it straightforward to subtract it as a contribution to background noise in the acquired spectrum. It is also very rigid which is an advantage during SXRF measurement, and tolerates exposure typically required for supporting histological analysis. However, as it blocks transmission of much of the hard X-ray beam, it is helpful to use a transparent support film for samples where analyte concentrations approaches the detection limits at the beamline. This permits a pair of detectors to be positioned, each at 90° to I_0, to maximise the solid angle over which fluorescence from the sample is acquired (Mosselmans et al., 2009; Collingwood and Adams, 2017).

To enable correlation with the MRI R_2 and R_2* maps, tissue sections corresponding to the higher resolution MRI images were mapped over the full slice area of interest, and the adjacent (glass-mounted) section which had been histochemically stained was used to confirm the area required. Rastering in the focused X-ray beam provided in-plane 60 × 60 µm pixels where the X-ray beam sampled the full depth of the tissue section; the acquisition rate corresponded to a 1 s dwell per point in the image matrix. A full SXRF spectrum was acquired for each pixel, and these spectra were processed using the open source software PyMCA (Solé et al., 2007), which was used to fit all detectable elements within the accessible energy range and compute the signal intensity from the primary fluorescence peak for each element. The spectrum in each pixel was normalised to the corresponding I_0 value to remove the effect of changing incident flux over the period of measurement, and the signal from a blank area on each quartz slide was used to correct for any difference in sample-detector distance. The resulting spectra were processed to produce precise maps of the normalized concentration distribution of the primary transition metals present in each tissue section (Finnegan, 2013).

2.6. Correlating SXRF and MRI images

The SXRF iron maps acquired from the 30 µm thick sections were correlated with the MRI microscopy data obtained with slightly lower (86 × 86 µm) in-plane spatial resolution and 150 µm thick virtual slices. By taking thinner sections for SXRF, this ensured that several serial cryosections could be well-matched to each virtual MRI slice. Image J was used to rotate the images from the different modalities to achieve a common orientation, and this was achieved by comparing

Table 2
Scan parameters for MRI relaxometry at 9.4 T for the low-spatial-resolution and high-spatial-resolution imaging of the tissue blocks. MSME = multi-slice multi-echo; MGE = multi-gradient-echo. T_R = repetition time. T_E = echo spacing.

Measurement: Parameter:	T_2 (low res)	T_2 (high res)	T_2* (low res)	T_2* (high res)
Resolution (µm)	195 × 195	86 × 86	195 × 195	86 × 86
Slice thickness (µm)	250	150	250	150
Scan sequence	MSME	MSME	MGE	MGE
Attenuators: A0, A1	16, 3	16, 3	22.5, -	22.5, -
T_R (ms)	7000	7000	3500	4000
T_E [T first echo] (ms)	7.248	9.783	6.0 [3.08]	6.0 [3.90]
No. of echoes	16	16	16	16
No. of averages	2	4	2	4
Scan time	22m24s	1h29m36s	11m12s	51m12s

anatomical features in the SXRF and MRI images, and microscope camera images of the stained and unstained SXRF section and the adjacent histochemically stained tissue sections. Factors that occasionally compromised correlation of the images included any misalignment of the block for sectioning, slight deformation of the tissue by the Fluorinert during MRI analysis, or sectioning artefacts such as cracks or folds in the unembedded tissue. This approach, in combination with the careful preservation of tissue architecture, made manual correlation viable at the level of individual brain regions.

2.7. Statistical analysis

SSPS Statistics Version 21 was used to carry out linear regression analysis, creating simple linear regression models to describe the relationship between the measured MRI parameters (dependent variables: R_2, R_2*, R_2') and the predictor (independent variable: iron). The correlation coefficient, r, described the linear relationship, and the goodness of fit was reported as r-squared. SSPS was used to calculate a p-value for the predictor in each case, testing for violation of the null hypothesis, that there was no dependence of each measured MRI parameter (R_2, R_2*, R_2') on iron, at a significance level of $p < 0.05$.

3. Results and discussion

Examples of matched SXRF and R_2 images, showing the approximate boundaries for segmentation, are given in Fig. 2, and the structures segmented for analysis are detailed in Table 3; those structures adjacent to the main regions of interest were segmented where possible. The correspondence between the SXRF and MRI images permitted determination of the relationship between the MR relaxation values and the associated iron concentration in each region. One section included elevated iron directly associated with a major blood vessel; the affected region was excluded from the analysis.

3.1. Calibration of SXRF maps

The iron concentration represented by one unit of normalised SXRF signal intensity was calculated for each sample by dividing the mean SXRF signal for that region by the mean bulk iron concentration measured in the adjacent tissue block. The mean and standard deviation for each sample was calculated and then averaged for all samples giving a mean of 7.3 ± 12% μg Fe / g hydrated tissue for every unit of normalised SXRF intensity.

3.2. The dependence of R_2, R_2*, and R_2' on iron concentration

Fig. 3 shows the mean iron concentration versus R_2 and R_2* for each of the main segmented regions from the correlated SXRF and MRI image data, for the pooled data, and separately for the grey matter (GM) and white matter (WM). The prediction bands show the range within which 95% of any new measurements would be expected to fall.

The linear regression analysis described in Fig. 3, and the results of this analysis set out in Table 4, produced the following equations relating R_2 and R_2* (s^{-1}) to iron concentration ([Fe] in μg/g, with an

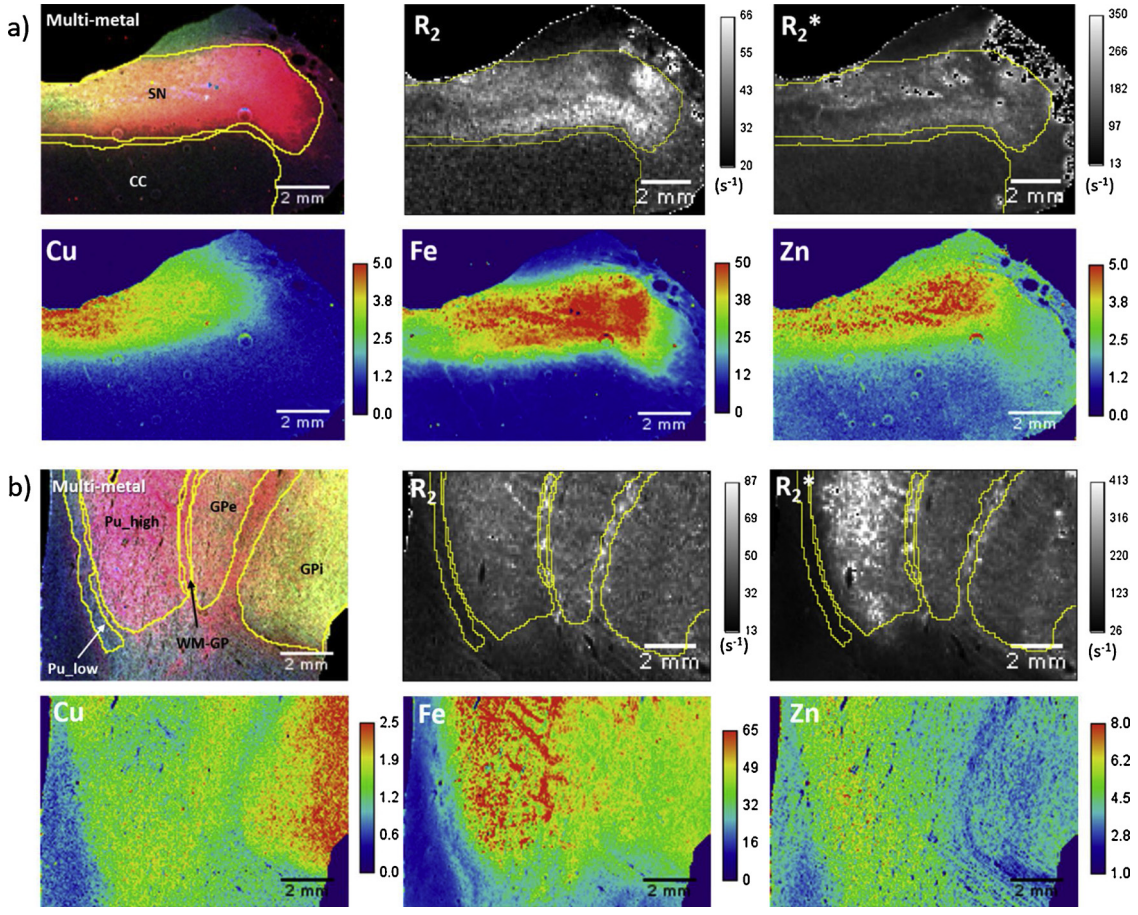


Fig. 2. Matched and segmented SXRF transition metal maps and MRI R_2 and R_2* maps from a) the substantia nigra and b) the globus pallidus regions in case AD2. During segmentation the intensity maps for the high abundance elements as well as the individual transition metals, were used to aid boundary identification. Here, RBG images are shown to illustrate how there are distinct distributions of Fe, Zn, and Cu at this level of structural organisation. In the multi-metal maps these are represented as Fe (red), Cu (green), Zn (blue). The accompanying scale bars show the computed R_2 and R_2* values for the MRI maps, and the temperature scale bars for the transition metal maps show the normalized fluorescence intensity. Labels for the segmented regions are defined in Table 3.

Table 3
Summary of the regions segmented in the SXRF and MRI R_2 maps.

Region	Main Structures	Additional Structures
Caudate Nucleus	caudate nucleus (CN); anterior limb of the internal capsule (AIC-CN); white matter medial to the caudate nucleus (WM-CN)	n/a
Putamen	putamen with high iron concentration (Pu_high); putamen with low iron concentration (Pu_low); white matter lateral to the putamen (Pu-WM)	Control sample only: anterior limb of the internal capsule (AIC-Pu)
Globus Pallidus	external globus pallidus (GPe); putamen with high iron concentration (Pu_high-GP); lamina of white matter separating the external globus pallidus and putamen (WM-GP)	Control sample only: internal capsule (IC); internal globus pallidus (GPi) AD sample only: putamen with low iron concentration (Pu_low-GP)
Substantia Nigra	substantia nigra (SN); cerebral crus (CC)	n/a

estimated experimental uncertainty of ± 12%:

$$R_2 = 0.072\,[Fe] + 20 \quad (2)$$

$$R_2^* = 0.34\,[Fe] + 37 \quad (3)$$

The linear relationship proved robust, regardless of whether the data were grouped by disease, or tissue type (grey or white matter). Furthermore, the slope and intercept of the fitted lines agree within error for each model for both R_2 and R_2*. In a prior study of the hippocampus (Antharam et al., 2012), we previously demonstrated that areas of increased iron concentration corresponded to increased R_2 and R_2* in matched MRI and SXRF maps at 14.1 T, but here the relationship was not quantified. Although a strong linear relationship has previously been shown between iron and R_2* at lower fields (between 1.5 T and 7 T (Yao et al., 2009)), this present study provides, to the best of our knowledge, the first demonstration of the linear relationship between iron concentration and R_2 and R_2* in human brain tissue at 9.4 T and the first demonstration, with quantified iron values, above 7 T.

In clinical MRI imaging the different relaxation rates of grey and white matter tissues provide contrast in the image and this is attributed to their differing fat and water content in addition to iron content. However, in this study the agreement of the linear relationship between iron and R_2 and R_2* for both grey and white matter suggests that at 9.4 T, iron is the most significant factor in determining the value of R_2 and R_2*. The r-squared values obtained in the regression analysis indicate that > 65% of variation in the data is accounted for by this linear relationship. The evidence for this has not always previously been apparent in studies including white matter (House et al., 2008), and here the inclusion of white matter regions with higher iron levels than typically observed in cortical regions may be a factor. The linear relationship we report at 9.4 T is not observed below a threshold of 100 µg/g, and this observation is in keeping with prior work at 4.7 T reporting a threshold of 55 µg/g for R_2 (House et al., 2007). We consider the relationship between R_2, iron, and field strength in the following section.

The effect of iron on R_2 increases linearly with field strength (B, Tesla), as formerly described empirically by Vymazal and co-workers (Eq. (4)). They derived this from iron and R_2 data measured at multiple field strengths (0.05 to 1.5 T) at 37 °C in primate brain tissue (Vymazal et al., 1996).

$$\text{slope} = 14.1 + 6.2B\ s^{-1}/mg/g \quad (4)$$

When Eq. (4) is solved for an imaging field of 9.4 T (400 MHz), it gives a slope of 0.0724 s^{-1}/µg/g. This compares extremely well with the gradient of Eq. (2) above, 0.072 ± 0.008 s^{-1}/µg/g, with no evidence of saturation of the field dependent R_2 increase at 9.4 T.

House and co-workers also compared their observations at 4.7 T to Vymazal's prediction and noted good agreement after accounting for differences in experiment design (House et al., 2007). Therefore, while the agreement we observe between our findings for R_2 and Vymazal's prediction is excellent, it is important to note differences in experiment design that may contribute experimental uncertainty in addition to ± 12% arising from calibration of the iron images with the SXRF data:

1. R_2 may be increased in tissue which has been frozen and defrosted (Vymazal et al., 1996), and the samples used to determine Eq. (4) were fresh compared with the defrosted post-mortem human brain used in the present study.
2. R_2 has been shown to decrease with temperature (Kamman et al., 1988) and Eq. (4) is for tissue at 37 °C compared for the present study performed at 2 °C.
3. The inter-echo time used in the sequence to obtain R_2 may influence the effect of iron content on R_2 (Vymazal et al., 1996).

The susceptibility related relaxation rate R_2* is generally understood to represent the combination of the transverse relaxation rate R_2 and the field inhomogeneity induced R_2'. R_2* is reportedly more sensitive to changes in tissue iron concentration than R_2 (Langkammer et al., 2010), and this is reflected in the present results (Fig. 3, Eq. (3)). The approximate mean R_2' was subsequently calculated for each segmented region, using Eq. (5):

$$R_2' = R_2^* - R_2 \quad (5)$$

and plotted against iron concentration as shown in Fig. 4 with the results of linear regression analysis for the combined and separated control and AD data, confirming a strong linear dependence of R_2', consistent with the earlier results for R_2 and R_2*. We note that the gradient for this relationship for R_2' is 3.75 times larger than the gradient for R_2 (Fig. 3, Eq. (2)). These gradients have been reported approximately equivalent at 3 T (Gelman et al., 1999), so these new data at 9.4 T indicate that not only is there a B-field-dependent contribution to the relationship between of R_2 with iron (Vymazal et al., 1996); there is also a field-dependent contribution arising from the dependence of R_2' on iron concentration. It is reasonable to assume a linear relationship between the magnitude of the field B and R_2', as this has previously been shown for the field-dependence of R_2* (Yao et al., 2009). The present result obtained at 9.4 T and the prior result from Gelman and co-workers at 3 T can then be used to compute the gradient (slope) for the dependence of R_2' on iron concentration at a particular imaging field B as follows:

$$\text{slope} = -51.1 + 34.4B\ s^{-1}/mg/g \quad (6)$$

It is long-postulated that MRI-detectable changes in iron concentration may aid diagnosis of neurodegenerative disorders, including AD (Antharam et al., 2012; Haacke et al., 2005; Langkammer et al., 2014; Bartzokis et al., 1994). In the present study, despite the strong linear relationships established with a very small sample size, the

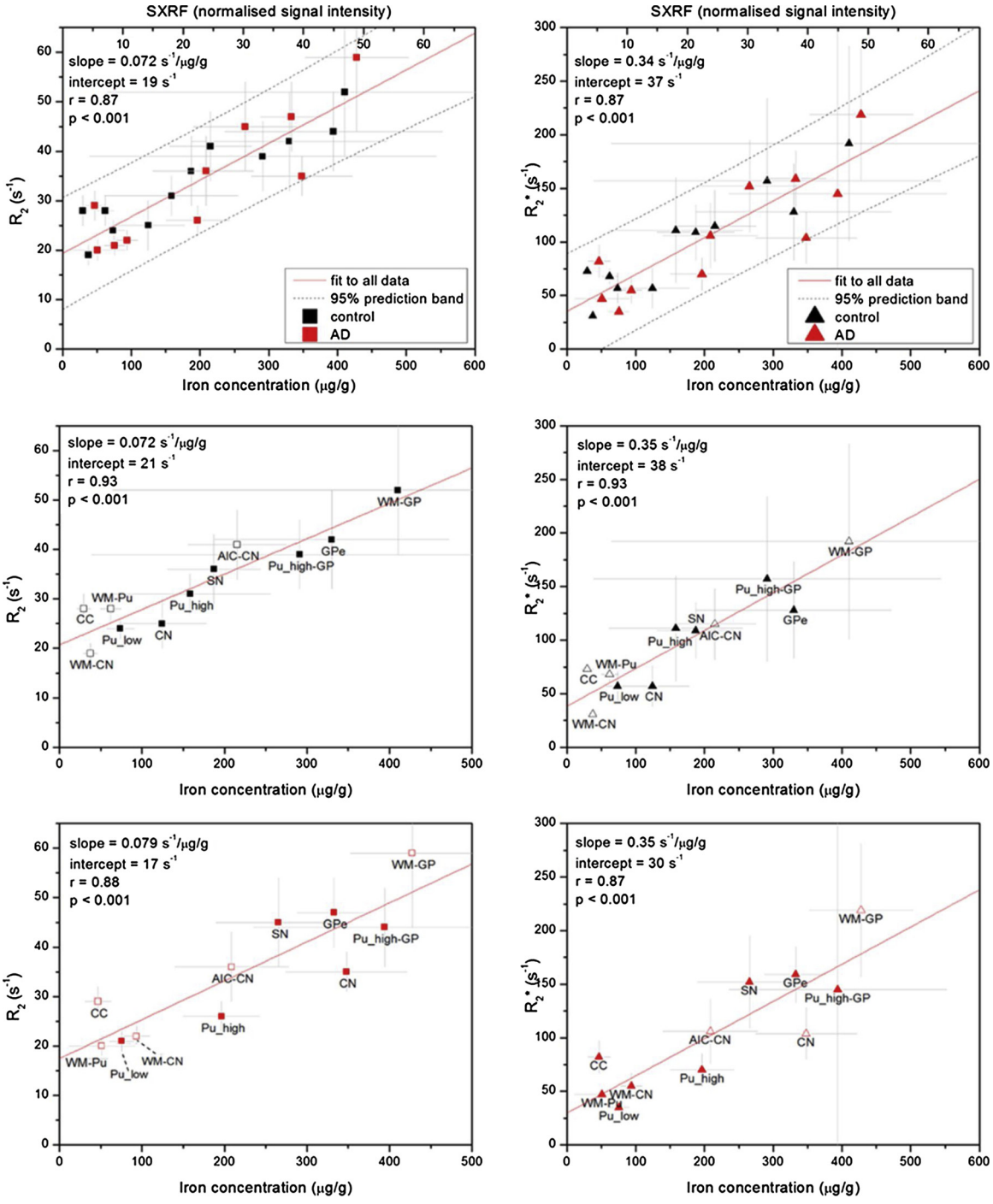


Fig. 3. Iron concentration versus R_2 and R_2* at 9.4 T. Results from linear regression analysis are shown in graphs a) and b) for the dependence of R_2 and R_2* respectively on iron concentration in the pooled control and AD data. The light grey error bars represent the standard deviation within each the segmented region, and are primarily a measure of signal heterogeneity rather than experimental uncertainty. The upper x-axis shows normalised SXRF iron signal intensity and the lower x-axis shows the calibrated iron concentration. The prediction bands show the region in which 95% of any new measurements would be predicted to fall. Graphs c) and d) show the dependence of R_2 and R_2* respectively on iron for control GM (filled symbol) and WM (open symbol) samples; e) and f) show the equivalent data from the AD cases. The results support a linear relationship, with $r > 0.85$ in all examples.

indications are that a substantial increase in tissue iron would be required to be reliably detected as a deviation from normal levels observed in cross-sectional studies, even at the highest clinically-available fields. The evaluation of multiple regions, and of more than one marker of iron status, offers scope to discriminate between disease states even in small cohorts (Visanji et al., 2013). Given the heterogeneity in normal regional iron concentration, it is likely that longitudinal imaging to track change in individuals may provide the greatest sensitivity and specificity to detect changes in the chemistry of the brain.

3.3. Method assumptions

3.3.1. ICP-MS and GFAAS determination of iron concentration are equivalent

As noted in Section 2.2, practical constraints in the present study resulted in most of the bulk analyses being performed using ICP-MS,

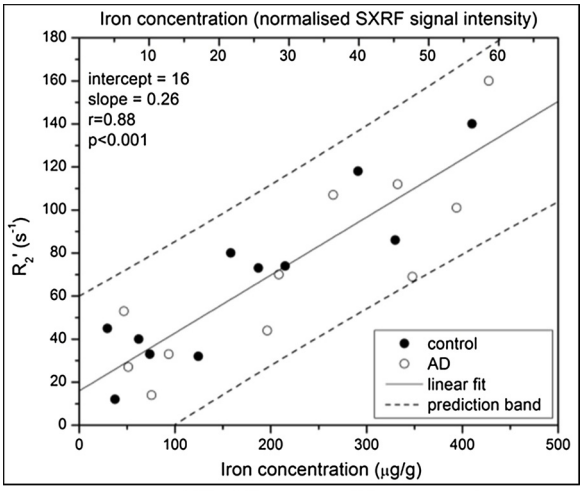
Table 4
Results of linear regression analysis of iron versus R_2 or R_2*. a) The linear relationship between iron and R_2. b) The linear relationship between iron and R_2*. The relationship is examined for the control and AD data separately and with both sets of data pooled. Data from grey and white matter regions is also examined separately. In all cases there a statistically significant, strong linear relationship. The r-squared values show that at least 67% of the variation in the data is explained by the linear relationship. All R_2 models show a slope and intercept which agree within error. The same is true for all of the fits to the R_2* data. *p < 0.05; **p < 0.01; ***p < 0.001.

a) Iron vs. R_2

Tissue regions	Disease	n	Slope (s^{-1}/(μg/g))	Intercept (s^{-1})	r	r^2	p
All	pooled	22	0.072 ± 0.008	19 ± 2	0.87	0.75	***
	Control	11	0.072 ± 0.009	21 ± 2	0.93	0.87	***
	AD	11	0.079 ± 0.012	17 ± 4	0.88	0.77	***
GM	Control	6	0.072 ± 0.011	19 ± 2	0.96	0.92	**
	AD	6	0.076 ± 0.027	16 ± 8	0.82	0.67	*
WM	Control	5	0.076 ± 0.013	22 ± 3	0.96	0.91	*
	AD	5	0.094 ± 0.016	18 ± 3	0.96	0.92	**

b) Iron vs. R_2*

Tissue regions	Disease	n	Slope (s^{-1}/(μg/g))	Intercept (s^{-1})	r	r^2	p
All	pooled	22	0.34 ± 0.04	37 ± 9	0.87	0.75	***
	Control	11	0.35 ± 0.05	38 ± 10	0.93	0.87	***
	AD	11	0.35 ± 0.07	30 ± 17	0.87	0.75	***
GM	Control	6	0.35 ± 0.10	35 ± 21	0.87	0.76	*
	AD	6	0.35 ± 0.12	16 ± 35	0.82	0.7	*
WM	Control	5	0.36 ± 0.06	41 ± 120	0.97	0.93	**
	AD	5	0.42 ± 0.07	33 ± 150	0.96	0.92	**



Disease	n	Slope (s^{-1}/(μg/g))	Intercept (s^{-1})	r	r^2	P
pooled	22	0.27 ± 0.03	16 ± 7	0.88	0.77	***
Control	11	0.28 ± 0.04	18 ± 9	0.92	0.84	***
AD	11	0.27 ± 0.05	12 ± 14	0.86	0.74	**

Fig. 4. Iron concentration versus approximate R_2'. The x-axis at the top of the graphs shows the normalised iron SXRF signal intensity and the lower axis shows the calibrated iron concentration. Simple linear regression analysis shows a strong (r > 0.85) linear relationship between iron concentration and R_2'. The prediction bands show where 95% of any new measurements are predicted to fall. The slope and the intercept of the fit agree within error for both the pooled and separated control and AD data, representing 22 samples from two control and three Alzheimer's disease cases, encompassing the regions detailed in Table 3. **p < 0.01; ***p < 0.001.

with the exception of the SN blocks which were analysed by GFAAS. In order for the equivalence of these measures to be a justified assumption, careful calibration and quantification were performed for both methods (Finnegan, 2013; Visanji et al., 2013). In each case, signal is obtained from the analyte following dissolution of the complete tissue block, rather than selectively sampling within a volume of interest, and there is no reason to expect any deviation in accuracy given that both processes included careful calibration. An extensive review of post-mortem iron quantification by Haacke and colleagues (Haacke et al., 2005), which is summarized in Table 3.2 in (Finnegan, 2013), includes reported values for these same regions of the brain obtained by both ICP-MS and atomic absorption spectroscopy (AAS). There is no systematic difference in the reported values as a function of analytical technique: in some cases AAS returns higher concentrations, in other cases ICP-MS is higher. We suggest that the greatest source of experimental uncertainty will be in the method of dissection, and that having a single team perform all the dissections in a consistent manner (as was the case for the present study) is a critical factor in minimising experimental uncertainty.

3.3.2. Adjacent tissue blocks for bulk and SXRF analysis have equivalent iron concentrations

The method of calibrating the SXRF maps assumes that the tissue samples measured with ICP-MS or GFAAS and the corresponding ROIs mapped by SXRF have an equal concentration of iron. The dissection of each block was carefully planned in order to best achieve this, for example, the substantia nigra shown in Fig. 1 (AD2) was bisected parallel to the plane of the image to obtain SNpc and SNpr in both blocks. Tissue samples were approximately 1 cm thick, with the centre of adjacent samples (for bulk iron concentration and SXRF) approximately 0.5–1 cm apart. The validity of the assumption of equivalent iron concentrations was tested for relative levels, not absolute concentrations, by calculating the ratio of AD to control iron concentration for the bulk tissue iron measurements and the mean relative iron concentration measured by SXRF mapping. The ratios were in good agreement [CN: bulk tissue iron 3.04 versus SXRF 2.80 (8% difference); Pu: bulk tissue iron 1.28 versus SXRF 1.24 (3% difference); SN: bulk tissue 1.50 versus SXRF 1.41 (6% difference)]. Agreement of these ratios within 10% indicates that the relative iron concentrations are well-preserved across the tissue volumes sampled.

3.3.3. SXRF and MRI slices can be correlated despite different thicknesses

The difference in SXRF (30 μm) and MRI (150 μm) slice thicknesses, despite similar in-plane resolution, means that the SXRF maps account for iron signal from approximately 20% of the corresponding MRI slice volume. The properties of the tissue precluded cutting significantly thicker sections for SXRF, and the signal recovery in the MRI would have been compromised if thinner slices had been obtained. Cutting up to five sections for SXRF from within each MRI slice accommodated minor misalignment of the tissue block, and provided one or more adjacent sections for staining to confirm tissue architecture. Although this means the matching between the SXRF and MRI is imperfect, the method did allow examination of the relationship between iron, R_2 and R_2^* in unfixed samples at higher spatial resolution than in most prior work, with the anatomical structures of interest substantially unaltered over the 150 μm length-scale. The spatial resolution made it viable to explore contrast variation within anatomically defined regions, reducing the need to attempt bulk dissection within subfields. Indeed the difficulty in precisely excising brain structures has been commented on in the literature (House et al., 2007). The scope for pixel-by-pixel correlation in the ROIs was explored for these datasets, incorporating a protocol to rescale the MRI data relative to the SXRF data to bring them into a shared matrix using Matlab. In practice this approach did not provide such a robust outcome as the method applied in the current study, which takes the average signal intensity value from segmented ROIs where each sampled area includes thousands of pixels. This approach is more robust and pragmatic in studies where sections are imperfectly matched, as it is less prone to distortions arising from the experimental uncertainties.

3.3.4. Approaches to quantifying tissue iron distribution

Evaluation of total iron concentration in adjacent tissue blocks was used here as a pragmatic method to estimate brain iron concentration distribution in the SXRF iron maps. This was successful, with an experimental uncertainty ± 12% that is equivalent to or is better than the accuracy typically achieved with SXRF reference foils for tissue samples due to issues with matrix matching (Collingwood and Davidson, 2014). It is technically possible to achieve fully quantitative SXRF mapping of elemental distributions where the phase contrast information can be measured to perform the necessary mass correction (Kosior et al., 2012), but this is not yet routinely available at SXRF beamlines. The rationale for using SXRF here is that it is non-destructive, has a sensitivity that increases with spatial resolution as it is a flux- (rather than mass-) limited technique, and permits simultaneous acquisition of a rich multi-element spectral image (Collingwood and Adams, 2017). There are several excellent alternative beam methods (which by contrast to SXRF are destructive), including laser ablation ICP-MS imaging and others reviewed elsewhere (Collingwood and Adams, 2017); for these alternatives the concentration detection limit decreases as the spatial resolution of the imaging is increased.

We observed distinct variations in iron distribution both between and within the primary regions studied. This marked heterogeneity of iron distribution within the sub-fields of the brain may in part account for wide variations in the experimental reports of healthy adult brain levels (Haacke et al., 2005), along with variations due to the analytical approach used.

In the study from Frisoni and co-workers: '*Imaging markers for Alzheimer disease: Which vs how*', a large number of candidate imaging markers for AD were evaluated, including volumetric MRI. They concluded that the way in which an imaging marker is measured is at least as important to its success as the marker itself (Frisoni et al., 2013). This would certainly apply to the measurement of tissue iron concentration by MRI.

4. Conclusion

A linear dependence of R_2, R_2* and R_2' on iron concentration was observed at 9.4 T, independent of disease state or tissue type. The gradient of the relationship between iron and R_2 agrees with the predicted relationship at 9.4 T, with no indication of saturation of the field dependent R_2 increase. Iron is the focus of the present study as it offers strong scope for clinical evaluation, but the approach may be used more widely to evaluate other elements in Alzheimer's and related disorders, and to test their relative impact on candidate imaging parameters including quantitative susceptibility mapping and other clinically applicable modalities.

Declarations of interest

None.

Ethical considerations

The work described involving human tissue has been carried out in accordance with The Code of Ethics of the World Medical Association (Declaration of Helsinki). The work in this project was done under multi regional ethics committee (MREC) approval for the project 'Metal-ion accumulation in neurodegenerative disease' (REC ref: 07/MRE08/12, Collingwood).

Data sharing

The source information for the data is available at http://wrap.warwick.ac.uk/60293/

Acknowledgements

This study received support from the Alzheimer's Society (PhD studentship: MEF, JFC, JD), and the EPSRC (grants EP/K035193/1 and EP/M028186/1). This work was carried out with the support of Diamond Light Source, under allocations SP1125 and SP7453. Our thanks to Drs Paul Quinn and Kalotina Geraki for assistance at I18. The development work for the MRI scans was performed in the McKnight Brain Institute at the National High Magnetic Field Laboratory's AMRIS Facility, which is supported by National Science Foundation Cooperative Agreement No. DMR-1157490 and the State of Florida. The MRI probe used in this research was obtained through the Birmingham Science City Translational Medicine: Experimental Medicine Network of Excellence project, with support from Advantage West Midlands (AWM).

References

Akatsu, H., Hori, A., Yamamoto, T., Yoshida, M., Mimuro, M., Hashizume, Y., Tooyama, I., Yezdimer, E.M., 2012. 'Transition metal abnormalities in progressive dementias. Biometals 25, 337–350.

Antharam, V., Collingwood, J.F., Bullivant, J.P., Davidson, M.R., Chandra, S., Mikhaylova, A., Finnegan, M.E., Batich, C., Forder, J.R., Dobson, J., 2012. High field magnetic resonance microscopy of the human hippocampus in Alzheimer's disease: quantitative imaging and correlation with iron. Neuroimage 59, 1249–1260.

Bartzokis, G., Tishler, T.A., 2000. MRI evaluation of basal ganglia ferritin iron and neurotoxicity in Alzheimer's and Huntingon's disease. Cell. Mol. Biol. (Noisy-le-grand) 46, 821–833.

Bartzokis, G., Aravagiri, M., Oldendorf, W.H., Mintz, J., Marder, S.R., 1993. Field-Dependent transverse relaxation rate increase may be a specific measure of tissue iron stores. Magn. Reson. Med. 29, 459–464.

Bartzokis, G., Sultzer, D., Mintz, J., Holt, L.E., Marx, P., Phelan, C.K., Marder, S.R., 1994. In vivo evaluation of brain iron in Alzheimer's disease and normal subjects using MRI. Biol. Psychiatry 35, 480–487.

Bartzokis, George, Sultzer, David, Cummings, Jeffrey, Holt, Lori E., Hance, DarwoodB., Henderson, Victor W., Mintz, Jim, 2000. In vivo evaluation of brain iron in alzheimer disease using magnetic resonance imaging. Achiv. Gen. Psychiatry 57, 47–53.

Bartzokis, G., Tishler, T.A., Shin, I.S., Lu, P.H., Cummings, J.L., 2004. Brain ferritin iron as a risk factor for age at onset in neurodegenerative diseases. Redox-Active Metals Neurol. Disord. 1012, 224–236.

Betts, M.J., Acosta-Cabronero, J., Cardenas-Blanco, A., Nestor, P.J., Duzel, E., 2016. High-resolution characterisation of the aging brain using simultaneous quantitative susceptibility mapping (QSM) and R2* measurements at 7T. Neuroimage 138, 43–63.

Bizzi, A., Brooks, R.A., Brunetti, A., Hill, J.M., Alger, J.R., Miletich, R.S., Francavilla, T.L., Di Chiro, G., 1990. Role of iron and ferritin in MR imaging of the brain: a study in primates at different field strengths. Radiology 177, 59–65.

Bondareff, W., Raval, J., Colletti, P.M., Hauser, D.L., 1988. Quantitative magnetic resonance imaging and the severity of dementia in Alzheimer's disease. Am. J. Psychiatry 145, 853–856.

Braak, H., Braak, E., 1991. Neuropathological stageing of Alzheimer-related changes. Acta Neuropathol. 82, 239–259.

Bulk, M., Abdelmoula, W.M., Nabuurs, R.J.A., van der Graaf, L.M., Mulders, C.W.H., Mulder, A.A., Jost, C.R., Koster, A.J., van Buchem, M.A., Natte, R., Dijkstra, J., van der Weerd, L., 2018. Postmortem MRI and histology demonstrate differential iron accumulation and cortical myelin organization in early- and late-onset Alzheimer's disease. Neurobiol. Aging 62, 231–242.

Collingwood, Joanna F., Adams, Freddy, 2017. Chemical imaging analysis of the brain with X-ray methods. Spectrochim. Acta Part B At. Spectrosc. 130, 101–118.

Collingwood, J.F., Davidson, M.R., 2014. The role of iron in neurodegenerative disorders: insights and opportunities with synchrotron light. Front. Pharmacol. 5, 191.

Collingwood, J.F., Mikhaylova, A., Davidson, M., Batich, C., Steirt, W.J., Terry, J., Dobson, J., 2005. *In situ* characterisation and mapping of iron compounds in Alzheimer's disease tissue. J. Alzheimer's Dis. 7, 267–272.

Collingwood, J.F., Chandra, S., Davidson, M., Mikhaylova, A., Eksin, T., Dobson, J., Forder, J., Batich, C., 2008. High-resolution magnetic resonance imaging to quantify relaxation parameters in Alzheimer's brain tissue. Alzheimers Dementia 4.

Collingwood, J.F., Finnegan, M.E., Arya, Z., Hagen, J.P., Chen, S., Chowdhury, A., Wayte, S., Ngandwe, E., Visanji, N.P., Dobson, J., Gowland, P.A., Hazrati, L.N., Hutchinson, C.E., 2014. MRI evaluation of the relationship between R2, R2*, and tissue iron in the human basal ganglia. In: ISMRM (Ed.), Joint Annual Meeting ISMRM-ESMRMB. International Society for Magnetic Resonance in Medicine, Madrid, Italy.

Connor, J.R., Snyder, B.S., Beard, J.L., Fine, R.E., Mufson, E.J., 1992. Regional distribution of iron and iron-regulatory proteins in the brain in aging and Alzheimers-disease. J. Neurosci. Res. 31, 327–335.

Cornett, C.R., Markesbery, W.R., Ehmann, W.D., 1998. Imbalances of trace elements related to oxidative damage in Alzheimer's disease brain. Neurotoxicology 19, 339–345.

Dedman, D.J., Treffry, A., Candy, J.M., Taylor, G.A.A., Morris, C.M., Bloxham, C.A., Perry, R.H., Edwardson, J.A., Harrison, P.M., 1992. Iron and aluminum in relation to brain ferritin in normal individuals and Alzheimers-disease and chronic renal-dialysis patients. Biochem. J. 287, 509–514.

Deibel, M.A., Ehmann, W.D., Markesbery, W.R., 1996. Copper, iron, and zinc imbalances in severely degenerated brain regions in Alzheimer's disease: possible relation to oxidative stress. J. Neurol. Sci. 143, 137–142.

Dexter, D.T., Carayon, A., Javoy-Agid, F., Agid, Y., Wells, F.R., Daniel, S.E., Lees, A.J., Jenner, P., Marsden, C.D., 1991. Alterations in the levels of iron, ferritin and other trace metals in Parkinson's disease and other neurodegenerative diseases affecting the basal ganglia. Brain 114 (Pt 4), 1953–1975.

Doan, N.T., Engvig, A., Zaske, K., Persson, K., Lund, M.J., Kaufmann, T., Cordova-Palomera, A., Alnaes, D., Moberget, T., Braekhus, A., Barca, M.L., Nordvik, J.E., Engedal, K., Agartz, I., Selbaek, G., Andreassen, O.A., Westlye, L.T., Initiative Alzheimer's Disease Neuroimaging, 2017. Distinguishing early and late brain aging from the Alzheimer's disease spectrum: consistent morphological patterns across independent samples. Neuroimage 158, 282–295.

Dobson, J., Grassi, P., 1996. Magnetic properties of human hippocampal tissue–evaluation of artefact and contamination sources. Brain Res. Bull. 39, 255–259.

Drayer, B., Burger, P., Darwin, R., Riederer, S., Herfkens, R., Johnson, G.A., 1986. MRI of brain iron. AJR Am. J. Roentgenol. 147, 103–110.

Dubois, Bruno, Feldman, Howard H., Jacova, Claudia, Cummings, Jeffrey L., DeKosky, Steven T., Barberger-Gateau, Pascale, Delacourte, André, Frisoni, Giovanni, Fox, Nick C., Galasko, Douglas, Gauthier, Serge, Hampel, Harald, Jicha, Gregory A., Meguro, Kenichi, O'Brien, John, Pasquier, Florence, Robert, Philippe, Rossor, Martin, Salloway, Steven, Sarazin, Marie, de Souza, Leonardo C., Stern, Yaakov, Visser, Pieter J., Scheltens, Philip, 2010. Revising the definition of Alzheimer's disease: a new lexicon. Lancet Neurol. 9, 1118–1127.

Dubois, B., Hampel, H., Feldman, H.H., Scheltens, P., Aisen, P., Andrieu, S., Bakardjian, H., Benali, H., Bertram, L., Blennow, K., Broich, K., Cavedo, E., Crutch, S., Dartigues, J.F., Duyckaerts, C., Epelbaum, S., Frisoni, G.B., Gauthier, S., Genthon, R., Gouw, A.A., Habert, M.O., Holtzman, D.M., Kivipelto, M., Lista, S., Molinuevo, J.L., O'Bryant, S.E., Rabinovici, G.D., Rowe, C., Salloway, S., Schneider, L.S., Sperling, R., Teichmann, M., Carrillo, M.C., Cummings, J., Jack Jr., C.R., Group Proceedings of the Meeting of the International Working, A. D, the American Alzheimer's Association on "The Preclinical State of, July, and U. S. A. Washington Dc, 2016. Preclinical Alzheimer's disease: definition, natural history, and diagnostic criteria. Alzheimers Dement. 12, 292–323.

Dusek, P., Bahn, E., Litwin, T., Jablonka-Salach, K., Luciuk, A., Huelnhagen, T., Madai, V.I., Dieringer, M.A., Bulska, E., Knauth, M., Niendorf, T., Sobesky, J., Paul, F., Schneider, S.A., Czlonkowska, A., Bruck, W., Wegner, C., Wuerfel, J., 2017. Brain iron accumulation in Wilson disease: a post mortem 7 Tesla MRI - histopathological study. Neuropathol. Appl. Neurobiol. 43, 514–532.

Finnegan, M.E., 2013. Investigation of the relationship between iron and high field MRI in healthy and Alzheimer's disease tissue. Ph.D. thesis. University of Warwick.

Frisoni, G.B., Bocchetta, M., Chetelat, G., Rabinovici, G.D., de Leon, M.J., Kaye, J., Reiman, E.M., Scheltens, P., Barkhof, F., Black, S.E., Brooks, D.J., Carrillo, M.C., Fox, N.C., Herholz, K., Nordberg, A., Jack Jr., C.R., Jagust, W.J., Johnson, K.A., Rowe, C.C., Sperling, R.A., Thies, W., Wahlund, L.O., Weiner, M.W., Pasqualetti, P., Decarli, C., 2013. Imaging markers for Alzheimer disease: which vs how. Neurology 81, 487–500.

Gallagher, J.J., Finnegan, M.E., Grehan, B., Dobson, J., Collingwood, J.F., Lynch, M.A., 2012. Modest amyloid deposition is associated with iron dysregulation, microglial activation, and oxidative stress. J. Alzheimer Dis. 28, 147–161.

Gao, L., Jiang, Z., Cai, Z., Cai, M., Zhang, Q., Ma, Y., Li, G., Zhao, F., Ma, Q., 2017. Brain iron deposition analysis using susceptibility weighted imaging and its association with body iron level in patients with mild cognitive impairment. Mol. Med. Rep. 16, 8209–8215.

Gellein, K., Flaten, T.P., Erikson, K.M., Aschner, M., Syversen, T., 2008. Leaching of trace elements from biological tissue by formalin fixation. Biol. Trace Elem. Res. 121, 221–225.

Gelman, N., Gorell, J.M., Barker, P.B., Savage, R.M., Spickler, E.M., Windham, J.P., Knight, R.A., 1999. MR imaging of human brain at 3.0 T: preliminary report on transverse relaxation rates and relation to estimated iron content. Radiology 210, 759–767.

Ghadery, C., Pirpamer, L., Hofer, E., Langkammer, C., Petrovic, K., Loitfelder, M., Schwingenschuh, P., Seiler, S., Duering, M., Jouvent, E., Schmidt, H., Fazekas, F., Mangin, J.F., Chabriat, H., Dichgans, M., Ropele, S., Schmidt, R., 2015. R2* mapping for brain iron: associations with cognition in normal aging. Neurobiol. Aging 36, 925–932.

Gossuin, Y., Burtea, C., Monseux, A., Toubeau, G., Roch, A., Muller, R.N., Gillis, P., 2004. Ferritin-induced relaxation in tissues: an in vitro study. J. Magn. Reson. Imaging 20, 690–696.

Graham, S.F., Nasaruddin, M.B., Carey, M., Holscher, C., McGuinness, B., Kehoe, P.G., Love, S., Passmore, P., Elliott, C.T., Meharg, A.A., Green, B.D., 2014. Age-associated changes of brain copper, iron, and zinc in Alzheimer's disease and dementia with Lewy bodies. J. Alzheimers Dis. 42, 1407–1413.

Haacke, E.M., Xu, Y.B., Cheng, Y.C.N., Reichenbach, J.R., 2004. Susceptibility weighted imaging (SWI). Magn. Reson. Med. 52, 612–618.

Haacke, E.M., Cheng, Y.C.N., House, M.J., Liu, Q., Neelavlli, J., Ogg, R.J., Khan, A., Ayaz, M., Kirsch, W., Obernaus, A., 2005. Imaging iron stores in the brain using magnetic resonance imaging. Magn. Reson. Imaging 23, 1–25.

Habes, M., Janowitz, D., Erus, G., Toledo, J.B., Resnick, S.M., Doshi, J., Van der Auwera, S., Wittfeld, K., Hegenscheid, K., Hosten, N., Biffar, R., Homuth, G., Volzke, H., Grabe, H.J., Hoffmann, W., Davatzikos, C., 2016. Advanced brain aging: relationship with epidemiologic and genetic risk factors, and overlap with Alzheimer disease atrophy patterns. Transl. Psychiatry 6, e775.

Hallgren, B., Sourander, P., 1958. The effect of age on the non-haemin iron in the human brain. J. Neurochem. 3, 41–51.

Hametner, S., Endmayr, V., Deistung, A., Palmrich, P., Prihoda, M., Haimburger, E., Menard, C., Feng, X., Haider, T., Leisser, M., Kock, U., Kaider, A., Hoftberger, R., Robinson, S., Reichenbach, J.R., Lassmann, H., Traxler, H., Trattnig, S., Grabner, G., 2018. The influence of brain iron and myelin on magnetic susceptibility and effective transverse relaxation - A biochemical and histological validation study. Neuroimage 179, 117–133.

Hare, D.J., Raven, E.P., Roberts, B.R., Bogeski, M., Portbury, S.D., McLean, C.A., Masters, C.L., Connor, J.R., Bush, A.I., Crouch, P.J., Doble, P.A., 2016. Laser ablation-inductively coupled plasma-mass spectrometry imaging of white and gray matter iron distribution in Alzheimer's disease frontal cortex. Neuroimage 137, 124–131.

Hopp, K., Popescu, B.F., McCrea, R.P., Harder, S.L., Robinson, C.A., Haacke, M.E., Rajput, A.H., Rajput, A., Nichol, H., 2010. Brain iron detected by SWI high pass filtered phase calibrated with synchrotron X-ray fluorescence. J. Magn. Reson. Imaging 31, 1346–1354.

House, M.J., St Pierre, T.G., Kowdley, K.V., Montine, T., Connor, J., Beard, J., Berger, J., Siddaiah, N., Shankland, E., Jin, L.W., 2007. Correlation of proton transverse relaxation rates (R2) with iron concentrations in postmortem brain tissue from Alzheimer's disease patients. Magn. Reson. Med. 57, 172–180.

House, M.J., Pierre, T.G.S., McLean, C., 2008. 1.4T study of proton magnetic relaxation rates, iron concentrations, and plaque burden in Alzheimer's disease and control postmortem brain tissue. Magn. Reson. Med. 60, 41–52.

House, M.J., Fleming, A.J., de Jonge, M.D., Paterson, D., Howard, D.L., Carpenter, J.P., Pennell, D.J., St Pierre, T.G., 2014. MApping iron in human heart tissue with synchrotron x-ray fluorescence microscopy and cardiovascular magnetic resonance. J. Cardiovasc. Magn. Reson. 16, 80.

Jack, Clifford R., Knopman, David S., Jagust, William J., Petersen, Ronald C., Weiner, Michael W., Aisen, Paul S., Shaw, Leslie M., Vemuri, Prashanthi, Wiste, Heather J., Weigand, Stephen D., Lesnick, Timothy G., Pankratz, Vernon S., Donohue, Michael C., Trojanowski, John Q., 2013. Tracking pathophysiological processes in Alzheimer's disease: an updated hypothetical model of dynamic biomarkers. Lancet Neurol. 12, 207–216.

Jensen, J.H., Chandra, R., 2000. Strong field behavior of the NMR signal from magnetically heterogeneous tissues. Magn. Reson. Med. 43, 226–236.

Kamman, R.L., Go, K.G., Brouwer, W., Berendsen, H.J.C., 1988. Nuclear magnetic resonance relaxation in experimental brain edema: effects of water concentration, protein concentration, and temperature. Magn. Reson. Med. 6, 265–274.

Kim, H.G., Park, S., Rhee, H.Y., Lee, K.M., Ryu, C.W., Rhee, S.J., Lee, S.Y., Wang, Y., Jahng, G.H., 2017. Quantitative susceptibility mapping to evaluate the early stage of Alzheimer's disease. Neuroimage Clin. 16, 429–438.

Kosior, E., Bohic, S., Suhonen, H., Ortega, R., Deves, G., Carmona, A., Marchi, F., Guillet, J.F., Cloetens, P., 2012. Combined use of hard X-ray phase contrast imaging and X-ray fluorescence microscopy for sub-cellular metal quantification. J. Struct. Biol. 177, 239–247.

Kumar, N., Rizek, P., Jog, M., 2016. Neuroferritinopathy: Pathophysiology, Presentation, Differential Diagnoses and Management. Tremor Other Hyperkinet. Mov. (N Y) 6, 355.

Laakso, M.P., Partanen, K., Lehtovirta, M., Hallikainen, M., Hanninen, T., Vainio, P., Riekkinen, P., Soininen, H., 1995. MRI of amygdala fails to diagnose early Alzheimer's disease. Neuroreport 6, 2414–2418.

ARTICLE IN PRESS

Langkammer, C., Krebs, N., Goessler, W., Scheurer, E., Ebner, F., Yen, K., Fazekas, F., Ropele, S., 2010. Quantitative MR imaging of brain iron: a postmortem validation study. Radiology 257, 455–462.
Langkammer, C., Schweser, F., Krebs, N., Deistung, A., Goessler, W., Scheurer, E., Sommer, K., Reishofer, G., Yen, K., Fazekas, F., Ropele, S., Reichenbach, J.R., 2012. Quantitative susceptibility mapping (QSM) as a means to measure brain iron? A post mortem validation study. Neuroimage 62, 1593–1599.
Langkammer, C., Ropele, S., Pirpamer, L., Fazekas, F., Schmidt, R., 2014. MRI for iron mapping in Alzheimer's disease. Neurodegener. Dis. 13, 189–191.
Liu, C., Li, C., Yang, J., Gui, L., Zhao, L., Evans, A.C., Yin, X., Wang, J., 2015. Characterizing brain iron deposition in subcortical ischemic vascular dementia using susceptibility-weighted imaging: An in vivo MR study. Behav. Brain Res. 288, 33–38.
Loeffler, D.A., Connor, J.R., Juneau, P.L., Snyder, B.S., Kanaley, L., Demaggio, A.J., Nguyen, H., Brickman, C.M., Lewitt, P.A., 1995. Transferrin and iron in normal, Alzheimers-disease, and Parkinsons-disease brain-regions. J. Neurochem. 65, 710–716.
Manova, E.S., Habib, C.A., Boikov, A.S., Ayaz, M., Khan, A., Kirsch, W.M., Kido, D.K., Haacke, E.M., 2009. Characterizing the mesencephalon using susceptibility-weighted imaging. AJNR Am. J. Neuroradiol. 30, 569–574.
McCrea, R.P.E., Harder, S.L., Martin, M., Buist, R., Nichol, H., 2008. A comparison of rapid-scanning X-ray fluorescence mapping and magnetic resonance imaging to localize brain iron distribution. Eur. J. Radiol. 68 S109-S13.
McKhann, Guy M., Knopman, David S., Chertkow, Howard, Hyman, Bradley T., Jack Jr., Clifford R., Kawas, Claudia H., Klunk, William E., Koroshetz, Walter J., Manly, Jennifer J., Mayeux, Richard, Mohs, Richard C., Morris, John C., Rossor, Martin N., Scheltens, Philip, Carrillo, Maria C., Thies, Bill, Weintraub, Sandra, Phelps, Creighton H., 2011. The diagnosis of dementia due to Alzheimer's disease: recommendations from the National Institute on Aging-Alzheimer's Association workgroups on diagnostic guidelines for Alzheimer's disease. Alzheimers Dementia 7, 263–269.
Morris, J.C., Blennow, K., Froelich, L., Nordberg, A., Soininen, H., Waldemar, G., Wahlund, L.O., Dubois, B., 2014. Harmonized diagnostic criteria for Alzheimer's disease: recommendations. J. Intern. Med. 275, 204–213.
Mosselmans, J.F., Quinn, P.D., Dent, A.J., Cavill, S.A., Moreno, S.D., Peach, A., Leicester, P.J., Keylock, S.J., Gregory, S.R., Atkinson, K.D., Rosell, J.R., 2009. I18—the microfocus spectroscopy beamline at the Diamond Light Source. J. Synchrotron Radiat. 16, 818–824.
Oakley, A.E., Collingwood, J.F., Dobson, J., Love, G., Perrott, H.R., Edwardson, J.A., Elstner, M., Morris, C.M., 2007. Individual dopaminergic neurons show raised iron levels in Parkinson disease. Neurology 68, 1820–1825.
Ordidge, R.J., Gorell, J.M., Deniau, J.C., Knight, R.A., Helpern, J.A., 1994. Assessment of relative brain iron concentrations using T2-weighted and T2*-weighted MRI at 3 Tesla. Magn. Reson. Med. 32, 335–341.
Pankhurst, Q., Hautot, D., Khan, N., Dobson, J., 2008. Increased levels of magnetic iron compounds in Alzheimer's disease. J. Alzheimers Dis. 13, 49–52.
Perls, M., 1867. Nachweis von Eisenoxyd in gewissen Pigmenten. Archiv für Pathologische Anatomie und Physiologie und für Klinische Medicin 39, 42–48.
Persson, N., Wu, J., Zhang, Q., Liu, T., Shen, J., Bao, R., Ni, M., Liu, T., Wang, Y., Spincemaille, P., 2015. Age and sex related differences in subcortical brain iron concentrations among healthy adults. Neuroimage 122, 385–398.
Pini, L., Pievani, M., Bocchetta, M., Altomare, D., Bosco, P., Cavedo, E., Galluzzi, S., Marizzoni, M., Frisoni, G.B., 2016. Brain atrophy in Alzheimer's Disease and aging. Ageing Res. Rev. 30, 25–48.
Samudralwar, D.L., Diprete, C.C., Ni, B.F., Ehmann, W.D., Markesbery, W.R., 1995. Elemental imbalances in the olfactory pathway in Alzheimer's disease. J. Neurol. Sci. 130, 139–145.
Schrag, Matthew, Mueller, Claudius, Oyoyo, Udochukwu, Smith, Mark A., Kirsch, Wolff M., 2011. Iron, zinc and copper in the Alzheimer's disease brain: A quantitative meta-analysis. Some insight on the influence of citation bias on scientific opinion. Prog. Neurobiol. 94, 296–306.
Solé, V.A., Papillon, E., Cotte, M., Walter, Ph, Susini, J., 2007. A multiplatform code for the analysis of energy-dispersive X-ray fluorescence spectra. Spectrochim. Acta Part B At. Spectrosc. 62, 63–68.
St Pierre, T.G., Clark, P.R., Chua-anusorn, W., 2004. Single spin-echo proton transverse relaxometry of iron-loaded liver. NMR Biomed. 17, 446–458.
Tan, H., Liu, T., Wu, Y., Thacker, J., Shenkar, R., Mikati, A.G., Shi, C., Dykstra, C., Wang, Y., Prasad, P.V., Edelman, R.R., Awad, I.A., 2014. Evaluation of iron content in human cerebral cavernous malformation using quantitative susceptibility mapping. Invest. Radiol. 49, 498–504.
Tang, X., Cai, F., Ding, D.X., Zhang, L.L., Cai, X.Y., Fang, Q., 2018. Magnetic resonance imaging relaxation time in Alzheimer's disease. Brain Res. Bull. 140, 176–189.
Tao, Y., Wang, Y., Rogers, J.T., Wang, F., 2014. Perturbed Iron Distribution in Alzheimer's Disease Serum, Cerebrospinal Fluid, and Selected Brain Regions: A Systematic Review and Meta-Analysis. J. Alzheimers Dis.
Thelwall, P.E., Shepherd, T.M., Stanisz, G.J., Blackband, S.J., 2006. Effects of temperature and aldehyde fixation on tissue water diffusion properties, studied in an erythrocyte ghost tissue model. Magn. Reson. Med. 56, 282–289.
Thompson, C.M., Markesbery, W.R., Ehmann, W.D., Mao, Y.X., Vance, D.E., 1988. Regional brain trace-element studies in Alzheimers-disease. Neurotoxicology 9, 1–8.
Ugarte, M., Grime, G.W., Lord, G., Geraki, K., Collingwood, J.F., Finnegan, M.E., Farnfield, H., Merchant, M., Bailey, M.J., Ward, N.I., Foster, P.J., Bishop, P.N., Osborne, N.N., 2012. Concentration of various trace elements in the rat retina and their distribution in different structures. Metallomics 4, 1245–1254.
van Duijn, S., Bulk, M., van Duinen, S.G., Nabuurs, R.J.A., van Buchem, M.A., van der Weerd, L., Natte, R., 2017. Cortical iron reflects severity of Alzheimer's disease. J. Alzheimers Dis. 60, 1533–1545.
Visanji, N.P., Collingwood, J.F., Finnegan, M.E., Tandon, A., House, E., Hazrati, L.N., 2013. Iron deficiency in parkinsonism: region-specific iron dysregulation in Parkinson's disease and multiple system atrophy. J. Parkinsons Dis. 3, 523–537.
Vymazal, J., Brooks, R.A., Zak, O., McRill, C., Shen, C., Dichiro, G., 1992. T1 and T2 of ferritin at different field strengths: effect on MRI. Magn. Reson. Med. 27, 368–374.
Vymazal, J., Brooks, R.A., Baumgarner, C., Tran, V., Katz, D., Bulte, J.W.M., Bauminger, E.R., DiChiro, G., 1996. The relation between brain iron and NMR relaxation times: an in vitro study. Magn. Reson. Med. 35, 56–61.
Wang, J.Y., Zhuang, Q.Q., Zhu, L.B., Zhu, H., Li, T., Li, R., Chen, S.F., Huang, C.P., Zhang, X., Zhu, J.H., 2016. Meta-analysis of brain iron levels of Parkinson's disease patients determined by postmortem and MRI measurements. Sci. Rep. 6, 36669.
Wisse, L.E., Biessels, G.J., Heringa, S.M., Kuijf, H.J., Koek, D.H., Luijten, P.R., Geerlings, M.I., Group Utrecht Vascular Cognitive Impairment Study, 2014. Hippocampal subfield volumes at 7T in early Alzheimer's disease and normal aging. Neurobiol. Aging 35, 2039–2045.
Wood, J.C., 2011. Impact of iron assessment by MRI. Hematology Am. Soc. Hematol. Educ. Program 2011, 443–450.
Yablonskiy, D.A., Haacke, E.M., 1994. Theory of NMR signal behavior in magnetically inhomogeneous tissues: the static dephasing regime. Magn. Reson. Med. 32, 749–763.
Yang, Ching-Hui, Hong, San-He, Jao, Jo-Chi, Tsai, Shu-Neng, Shiao, Chia-Chi, Yeung, Kwok-Wan, Chen, Po-Chou, 2013. Correlation between SPGR MR signal intensity and iron concentration: Phantom study. Biomark. Genom. Med. 5, 39–43.
Yao, B., Li, T.Q., Gelderen, P., Shmueli, K., de Zwart, J.A., Duyn, J.H., 2009. Susceptibility contrast in high field MRI of human brain as a function of tissue iron content. Neuroimage 44, 1259–1266.